Asian Journal of Chemistry; Vol. 38, No. 3 (2026), 801-814
ASIAN JOURNAL OF CHEMISTRY
https://doi.org/10.14233/ajchem.2026.35239

# Synthesis and Evaluation of SrO-Doped Hydroxyapatite Nanoparticle Hydrogels for Bone Regeneration

M. BALAKRISHNAN, P. JAYASUDHA and P.R. BHALAJI*

Department of Chemistry, Government Arts College for Men, Krishnagiri-635001, India

*Corresponding author: E-mail: prbhalaji@yahoo.in

*Received*: 12 November 2025 *Accepted*: 13 February 2026 *Published online*: 6 March 2026 AJC-22300

Hydrogels are multifunctional biomaterials widely utilised in biomedical applications owing to their biocompatibility, water retention capabilities and adjustable properties. Nonetheless, their restricted mechanical strength and bioactivity limit their application in bone tissue engineering. Present study focused on the development and evaluation of SrO-doped hydroxyapatite nanoparticles (SrO–HA) integrated into a polyvinyl alcohol/carboxyl methyl chitosan (PVA/CMC) hydrogel matrix to improve mechanical and osteogenic properties. The SrO@HA/PVA/CMC composite hydrogels were synthesised through a freeze-thaw physical crosslinking method and characterised to assess the porosity, swelling behaviour, ion release and biomineralisation, utilizing SEM, EDS and FTIR techniques. The biocompatibility and osteogenic potential were evaluated using rBMSCs *via* CCK-8 assays, alkaline phosphatase activity measurement and alizarin red staining. The hydrogels exhibited an interconnected porous structure, characterised by improved mechanical stability and sustained release of strontium ions. Elevated concentrations of SrO–HA (2%, 4% and 10%) enhanced biomineralisation and osteogenic differentiation, with the 4% and 10% hydrogels exhibiting superior efficacy. Sustained ion release facilitated rBMSC proliferation, increased ALP activity and resulted in significant extracellular matrix mineralisation. The biomimetic characteristics of SrO–HA, along with the three-dimensional porous structure of the hydrogels, facilitated these effects. The hydrogels facilitated apatite formation upon incubation in simulated body fluid, confirming their biomineralisation potential. The results indicate the possibility of SrO@HA/PVA/CMC composite hydrogels in bone tissue engineering.

**Keywords: Carboxyl methyl chitosan, Hydrogel, Hydroxylapatite, Polyvinyl alcohol, Strontium.**

## INTRODUCTION

Hydrogels are three-dimensional, cross-linked polymeric networks capable of absorbing and retaining substantial quantities of water or biological fluids [1,2]. Their soft, elastic and highly hydrated properties render them appropriate for various biomedical applications such as wound dressing, drug delivery and tissue engineering [3,4]. Carboxyl methyl chitosan (CMC), a derivative of the natural polysaccharide chitosan, is notable for its biocompatibility, biodegradability and capacity to improve cell adhesion and proliferation. Nonetheless, the inadequate mechanical strength presents a limitation that requires attention [5,6].

Polyvinyl alcohol (PVA) is a synthetic polymer utilised for the production of hydrogels, which exhibit favourable mechanical properties and water-binding capacity. PVA is a versatile and biocompatible material commonly utilised in biomedical applications, attributed to its superior film-forming, emulsifying and adhesive characteristics. PVA can be integrated with various polymers, metal ions and biomolecules using different processing methods to develop PVA-based composites that demonstrate superior mechanical properties, biocompatibility and non-toxicity [7,8]. The combination of carboxyl methyl chitosan and polyvinyl alcohol yields hydrogels that exhibit enhanced mechanical stability and functionality, rendering them appropriate for various biomedical applications, including wound dressing, tissue engineering and drug delivery [9-12].

Hydrogels based on PVA can be synthesised using different types of cross-linking techniques such as chemical, physical and radiation-induced methods. Chemical cross-linking frequently employs potentially toxic agents such as glutaraldehyde, dye glycosides or boric acids as cross-linkers. The complete removal of these agents can be difficult and any

residual traces may lead to cytotoxicity [13-15]. The freeze-thaw treatment facilitates the formation of PVA hydrogels *via* reversible physical cross-linking, thereby mitigating the potential cytotoxicity linked to the use of cross-linking agents. The brittleness and inadequate mechanical strength of freeze-thaw composite PVA/CMC hydrogels considerably restrict their use in the biomedical sector. Researchers have recently integrated hydrated polymers and doped nanoparticles into PVA/CMC systems to improve the mechanical properties and functionality of these hydrogels [9,11,16,17].

For bone tissue engineering applications, a naturally occurring calcium phosphate mineral is a popular biomaterial due to its superior osteoconductivity, biocompatibility and chemical resemblance to the mineral component of bone [18]. The integration of hydroxyapatite nanoparticles into PVA/CMC hydrogels enhances the mechanical strength, bioactivity and bone regenerative capacity. The incorporation of hydroxyapatite enhances the capacity of hydrogel to support and promote bone tissue regeneration, positioning it as a promising material for orthopedic and dental applications [14,19-22].

Strontium oxide (SrO) is a significant inorganic component that can be integrated into hydrogel systems. SrO stimulates osteoblast activity, inhibits osteoclast function and promotes bone formation, thus serving as a valuable component in bone tissue engineering applications [23]. The addition of SrO to the hydrogel matrix may enhance bone tissue regeneration outcomes. SrO enhances the osteogenic differentiation of stem cells and improves bone regenerative potential, positioning SrO-doped hydrogel as a promising candidate for orthopedic and dental applications. Thus, the incorporation of nano-hydroxyapatite, a calcium phosphate ceramic that replicates the mineral phase of natural bone, enhances the bioactivity and osteoconductive properties of the hydrogel [24-26].

Keeping in view of facts, an attempt is made to synthesise and characterise new SrO-loaded HA/PVA/CMC (SrO@HA/PVA/CMC) composite hydrogel. The hydrogel was synthesised by amalgamation polymers and incorporating a SrO–HA filler, which is anticipated to improve its bioactivity and bone regenerative capacity.

## EXPERIMENTAL

The chemicals *viz*. nitrate tetrahydrate ($Ca(NO_3)_2{\cdot}4H_2O$), strontium nitrate ($Sr(NO_3)_2$), diammonium hydrogen phosphate ($(NH_4)_2HPO_4$), sodium hydroxide ($NH_4OH$), polyvinyl alcohol (PVA), carboxymethyl cellulose (CMC) were procured from Sigma Aldrich chemicals, USA. Deionised water and all analytical-grade solvents were acquired and utilised without additional treatment.

**Preparation of SrO@HA composites:** In the conventional synthesis, SrO@HA composites can be produced *via* a wet chemical co-precipitation technique. Generally, approximately 4.14 g of $Ca(NO_3)_2{\cdot}4H_2O$ and a determined quantity of $Sr(NO_3)_2$ equal to 10%, molar substitution of calcium (0.84 g for 10% Sr) was individually dissolved in distilled water. The solutions were mixed and stirred at about 50-60 ºC, followed by the gradual addition of 1.74 g of $(NH_4)_2HPO_4$ solution while stirring. The pH was maintained around 10 using $NH_4OH$ solution. The mixture was stirred for 6 h to precipitate the Sr-doped hydroxyapatite and then left untouched for 24 h. Finally, the product was filtered, dried at 110 ºC and calcined at 600 ºC for 3 h to enhance the crystallinity and phase purity.

**Preparation of PVA/CMC hydrogel**: The CMC/PVA hydrogels can be obtained using several free-threw cycles. The PVA (0.9 g) was dissolved in 50 mL DI water at 90 ºC while stirring for 2 h to achieve a homogenous solution. Separately, CMC (0.1 g) was solubilised in 20 mL of water at 70 ºC for 4 h and then added dropwise slowly into the PVA solution and agitated at 70 ºC for an additional 4 h to ensure thorough mixing. The hydrogel structure was created by pouring the solution into molds and subjecting it to 3 to 5 freeze-thaw cycles; each cycle involves freezing at approximately -20 ºC for 12 h, followed by thawing at room temperature (~25 ºC) for 6 h. The produced hydrogels are subsequently extracted from the molds, thoroughly washed in DI water for 24 h to eliminate soluble constituents *via* lyophilisation.

**Preparation of SrO@HA/PVA/CMC composite hydrogel:** The synthesis of the SrO@HA/PVA/CMC composite hydrogel incorporates pre-synthesised SrO@HA nanoparticles into the PVA/CMC polymer matrix prior to cross-linking. The measured SrO@HA powder was initially introduced to a minimal volume of water and exposed to ultrasonication for 60 min to ensure effective deagglomeration of the particle clusters. The stabilised nanoparticle suspension was gradually incorporated into the homogenised PVA/CMC polymer solution with gentle stirring for 4 h to obtain a homogeneous suspension. The resultant nanocomposite mixture was casted into molds, succeeded by the essential physical cross-linking process employing 3-5 freeze-thaw cycles (generally freezing at -20 ºC for 12 h and thawing at 25 ºC for 10 h). Finally, the cross-linked composite hydrogels were extracted, thoroughly rinsed in DI water for 24 h to eliminate soluble, uncross-linked polymers.

**Characterisation:** The morphology of the hydrogel nanocomposites was examined using a cold-field emission scanning electron microscope (Hitachi SU8600). Before imaging, the hydrogel was swiftly quenched in liquid nitrogen and then freeze-dried for 24 h at -20 ºC to maintain its three-dimensional architecture. The freeze-dried samples were then sputter-coated with gold and analysed at an accelerating voltage of 10 kV. The nanocomposites hydrogel functional groups were analysed using FT-IR analysis (Thermo Nicolet-IS-50) and the spectral range analysed were 4000 to 400 $cm^{-1}$. The crystalline structure of the prepared HA, PVA/CMC and 2%, 4% and 10% strontium oxide doped hydroxyapatite (SrO @HA/PVA/CMC matrix were confirmed X-ray diffractometer (MiniFlex-600, Rigaku Co., Japan).

**Energy spectrometer scanning (EDS):** Freeze-dried hydrogels (PVA/CMC and SrO@HA/PVA/CMC) underwent elemental analysis using EDS utilizing (Oxford INCA x-act). Point and mapping investigations were conducted to ascertain the distribution and concentration of C, O and P inside the hydrogel structures. A comparative examination of the elemental data was performed to verify the effective integration of SrO–HA nanoparticles into the PVA/CMC hydrogel matrix.

**Density and porosity of hydrogel:** The interaction porosity of each sample was measured using the liquid displacement technique [27]. Before immersion, the initial volume ($V_o$) and weight ($W_o$) were precisely quantified. The samples were immersed in pure ethanol for 1, 4, 6, 8, 16, 24, 30, 45 and 60 min. Until a steady weight ($W_1$) was reached, the samples were weighed at each interval. The porosity (%) was calculated from the following formula:

$$\text{Porosity } (\%) = \frac{W_o - W_1}{\rho \text{ ethanol} \times V_o} \times 100 \quad (1)$$

where ρ is the density of ethanol and the density of hydrogel (d) was computed with eqn. 2:

$$d = \frac{W_o}{V_{oa}} \quad (2)$$

**Swelling degree of hydrogel:** The freeze-dried hydrogels were weighed ($M_1$) and then immersed in ultra-pure water. At set time intervals, they were removed, surface water was wiped off and weighed again until a constant weight ($M_2$) was reached. The equilibrium swelling ratio (%) was calculated using the formula:

$$\frac{M_2 - M_1}{M_1} \times 100\% \quad (3)$$

**Variation of pH in hydrogels:** The hydrogel was immersed in PBS in a centrifuge tube and incubated at 37 ºC to monitor pH changes. pH measurements were taken at specified intervals: 0.3, 0.5, 1, 2, 4, 6, 8, 10, 16, 20, 24 and 36 h, utilizing a specialised pH detector.

**Detection of sustained-release ions in hydrogels:** The hydrogels were placed in bottles of ultrapure water and allowed to incubate at 37 ºC. The concentration of SrO ions in each hydrogel sample ($W_1$ – $W_5$) was evaluated at intervals of 1, 5, 10, 15, 20, 25 and 30 days. The change in SrO ion concentration for each sample (WX) was determined using the following formula:

$$(WX)\ (\%) = \frac{WX - WX\text{-}1}{WX\text{-}1} \times 100 \quad (4)$$

where WX denotes the strontium ion concentration at a specific time point, while WX-1 indicates the concentration at the prior time point.

**Analysis of moisture level:** To ascertain the water content of the hydrogel, surface moisture was first eliminated using absorbent paper and the hydrogel was then weighed ($W_1$) [28]. The sample was then positioned in a drying oven set at 70 ºC for different periods (0.5-60 min) until a stable dry weight ($W_2$) was attained. Eqn. 5 was used to determine the moisture content %:

$$\text{Moisture content } (\%) = \frac{W_1 - W_2}{W_1} \times 100 \quad (5)$$

**Properties of biomineralisation:** During a 14-day incubation period, sterilised hydrogels were submerged in a simulated bodily fluid (SBF) in a temperature-controlled environment kept at 37 ºC. The SBF was renewed every 48 h to ensure proper mineralisation. After incubation, hydrogels were washed with ultrapure water to eliminate any remaining salts. Following freeze-drying, the elemental composition and content of the mineralised hydrogels were investigated using SEM combined with EDX.

***In vitro* bone mineralisation examination:** *In vitro* investigations were performed employing rat bone marrow mesenchymal stem cells (rBMSCs) to evaluate the bone mineralisation characteristics of the hydrogels. The alkaline phosphatase (ALP) staining and alizarin red staining were used to assess the impact of the hydrogels on bone mineralisation. Following the reported method [25], an extraction solution was formulated by separately immersing PVA/CMC, 2% SrO@HA/PVA/CMC, 4% SrO@HA/PVA/CMC and 10% SrO@HA/PVA/CMC hydrogels in rBMSC-specific media. Following a 24 h incubation at 37 ºC and 300 rpm, the extracts were harvested and filtered using a 0.25 μm sterile filter. The obtained extracts were then diluted 1:10 with new rBMSC-specific media to produce a conditioned medium and then kept at 4 ºC.

**Biocompatibility assay:** To evaluate *in vitro* biocompatibility, 96-well plates were seeded with 5000 cells per well. After 24 h of cell attachment, the culture medium was substituted with a conditioned medium from each hydrogel sample. Incubation was performed under standard cell culture conditions. On days 1, 4 and 7, the medium was discarded and 10 μL of 10% CCK-8 solution diluted in 90 μL of fresh medium was introduced to each well. Cell proliferation was assessed by measuring the absorbance of the supernatant at 450 nm following a subsequent 2 h incubation at 37 ºC.

**AO/EtBr staining assay:** The AO/EtBr staining assay was conducted to evaluate the cell viability by differentiating between viable and non-viable cells. At 1, 4 and 7 days following the introduction of osteogenic differentiation using hydrogels, the culture medium was discarded and the cells were rinsed twice with 1x PBS. Subsequently, the cells were trypsinised, collected *via* centrifugation at 500 x g for 3 min and resuspended in PBS. A working solution of acridine orange/ethidium bromide (AO/EtBr) was formulated at a concentration of 0.5 μg/mL. An equivalent volume of the working solution was incorporated into the cell suspension. Following a 5 min incubation, the stained cells were examined with a fluorescence microscope.

**Alkaline phosphatase (ALP) staining:** rBMSCs were inoculated at a density of $1 \times 10^5$ cells per well in 24-well plates and maintained in a specialised rBMSC medium. Following 24 h to facilitate cell attachment, the medium was substituted with the corresponding conditioned media. The cells were subsequently cultured for one and two weeks in a cell culture incubator. The ALP activity was evaluated utilising a BCIP/NBT chromogenic kit (name). Cells were washed with PBS, fixed using 4% paraformaldehyde for 20 min and then incubated with the BCIP/NBT working solution for 2 h at room temperature. The reaction was concluded by rinsing with distilled water. ALP activity was visualised and documented with an inverted microscope.

**Alizarin red staining:** Cells were plated at a density of $1 \times 10^5$ cells per well in 24-well plates and maintained in a specialised rBMSC medium. Following a 24 h incubation period to facilitate cell adhesion, the medium was substituted with a conditioned medium according to the specific experimental conditions. The cells were subsequently cultured for

2 weeks. Alizarin red staining was conducted to evaluate mineralisation. Cells were washed with PBS and fixed using 4% paraformaldehyde for 20 min and subsequently washed again with PBS. Then, 0.5 mL of 3% alizarin red staining solution was added to each well to ensure complete coverage. Following a 40 min incubation at room temperature, the staining solution was discarded and the wells were washed three times with PBS. Mineralised nodules were visualised and documented utilizing an inverted microscope.

**Statistical analysis**: Data are expressed as mean ± standard deviation (SD) from triplicate trials. The statistical significance was assessed using t-tests, with $p < 0.05$ being statistically significant.

## RESULTS AND DISCUSSION

**Strontium oxide-doped-HA:** SrO–HA was synthesised *via* a magnetic stirring-ion exchange method. SEM analysis demonstrated a clear morphological transformation resulting from strontium doping. Undoped HA demonstrated a rod-like morphology, averaging 80 nm in length and 35 nm in width, indicative of its anisotropic crystal growth (Fig. 1a). In contrast, SrO–HA exhibited a significant transition to a more spherical or quasi-spherical morphology, with an average diameter of approximately 60 nm (Fig. 1b). The morphological change is due to the incorporation of SrO ions into the hydroxyapatite lattice. The greater ionic radius of strontium ions relative to calcium ions likely interferes with the standard crystal growth process, resulting in lattice distortions and a departure from the usual anisotropic growth pattern. The ionic mismatch induces strain in the crystal lattice, obstructing preferential growth along a specific axis and encouraging more isotropic growth, which leads to the observed spherical morphology [29]. The particle size of SrO–HA increased but remained within the nanoscale range, which is significant for various reasons. Nanoscale particles typically demonstrate improved biocompatibility and cellular interactions. Furthermore, the reduced size enhances cellular uptake, which is essential for successful bone tissue regeneration. The nanoscale dimensions facilitate improved dispersion within the hydrogel matrix, resulting in a more homogeneous and stable composite material [30].

**Synthesised hydrogel of SrO@HA/PVA/CMC:** The composite hydrogels of SrO@HA/PVA/CMC, consisting of SrO–HA nanoparticles, PVA and CMC, were synthesised using a repeated freeze-thaw physical crosslinking technique (Fig. 2a-d). Visual observation indicated a progressive reduction in optical transparency from the control PVA/CMC hydrogel to the 2%, 4% and 10% (w/v) SrO–HA-incorporated hydrogels, along with a colour change from translucent white to opaque white and a modification in the hydrogel edge from sharp to slightly blurred. SEM investigation demonstrated unique three-dimensional interconnected porosity architecture across all hydrogel samples. The control PVA/CMC hydrogel had a coarse porous structure characterised by large, irregularly shaped pores (average pore size: 150 ± 10 μm), but the addition of SrO–HA nanoparticles markedly modified the pore morphology. The SrO@HA/PVA/CMC composites exhibited a denser and more interconnected porous structure with smaller, consistently distributed pores. The tendency was apparent with increasing SrO–HA concentration, yielding average pore diameters of 120 ± 8 μm, 90 ± 5 μm and 70 ± 3 μm for 2%, 4% and 10% SrO@HA/PVA/CMC hydrogels, respectively. The decrease in pore size is due to the robust interactions between the SrO@HA nanoparticles and the polymer matrix. The inclusion of SrO@HA nanoparticles likely promoted the development of a denser network by establishing strong ionic and hydrogen bonding contacts with the hydroxyl and carboxyl groups of PVA and CMC, respectively, during the freeze-thaw cycles. The improved intermolecular contact facilitated the construction of polymer chains, leading to a denser and more linked network with reduced pore size.

**EDS analysis of the hydrogels:** EDS analysis was performed to determine the elemental composition of PVA/CMC

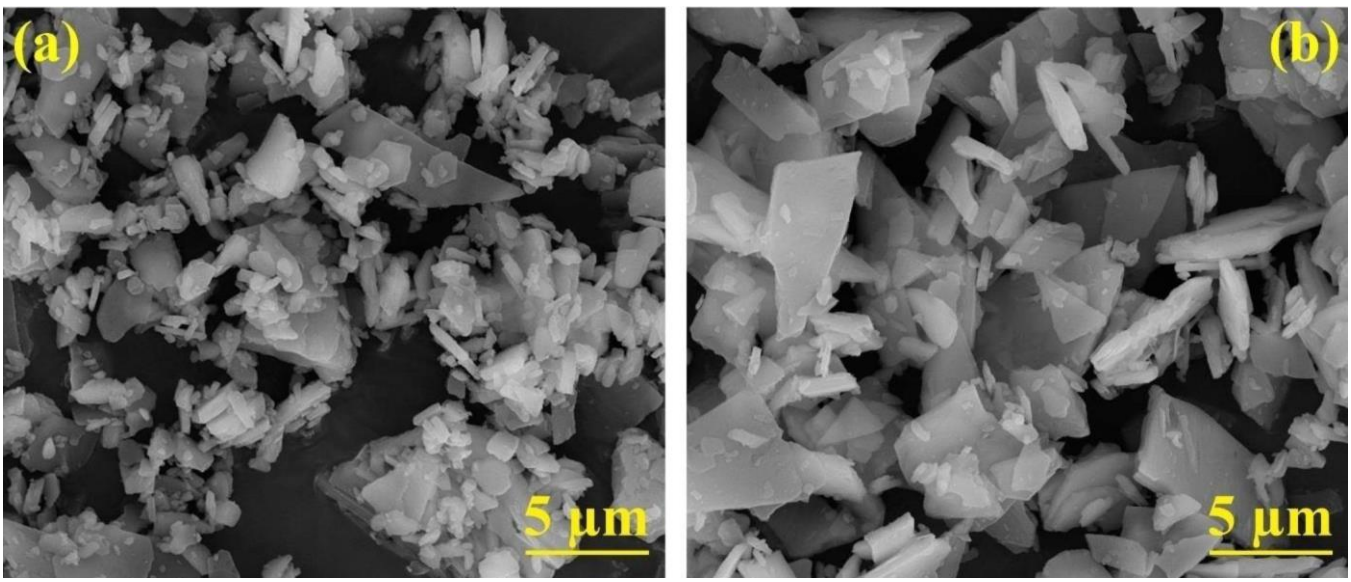


Fig. 1. (a) Scanning electron microscopy (SEM) image of hydroxyapatite (HA) (b) SEM image of strontium oxide-doped hydroxyapatite (SrO–HA)

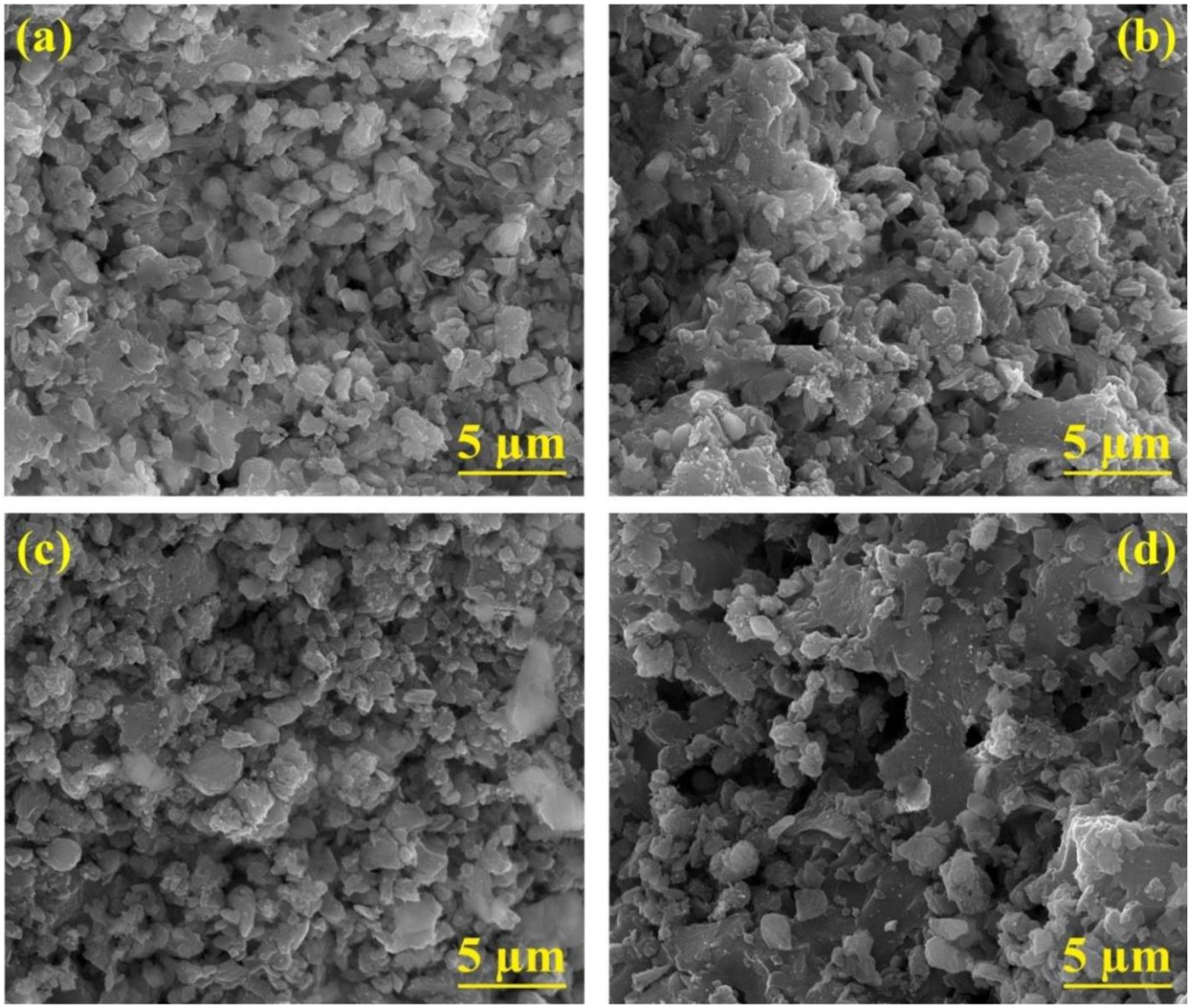


Fig. 2. SEM image of (a) polyvinyl alcohol/carboxymethyl cellulose (PVA/CMC) hydrogel, (b) 2% SrO@HA/PVA/CMC composite hydrogel, (c) 4% SrO@HA/PVA/CMC composite hydrogel, (d) 10% SrO@HA/PVA/CMC composite hydrogel

and SrO@HA/PVA/CMC hydrogels, which are potential biomaterials for bone tissue engineering (Fig. 3). The EDS spectra of the PVA/CMC hydrogel displayed typical peaks for C, O and N, aligning with the anticipated composition of the component polymers. In contrast, the SrO@HA/PVA/CMC hydrogel exhibited distinct peaks corresponding to Sr, Ca and P, therefore definitively validating the effective integration of SrO and HA nanoparticles into the hydrogel matrix. The integration of SrO and HA is essential for bone regeneration applications since they are recognised for promoting osteogenesis and improving biocompatibility [29,31]. The identification of Sr and the measured Ca/P ratio in the SrO@HA/PVA/CMC hydrogel confirmed the existence of both SrO and HA constituents inside the composite material. The results provide substantial proof of the effective synthesis of the SrO@HA/PVA/CMC composite hydrogel, a viable option for bone tissue engineering applications.

**FTIR analysis:** FTIR spectroscopy was used to examine the chemical interactions in the prepared PVA/CMC hydrogel and its SrO–HA-doped variants. All spectra displayed distinctive peaks corresponding to the functional groups of the component polymers (Fig. 4). A wide and pronounced band detected in the 3500-3000 $cm^{-1}$ range across all samples was ascribed to the overlapping stretching vibrations of O–H groups from PVA and CMC, with N–H stretching vibrations from the amide groups in the CMC backbone. The peak at about 2940 $cm^{-1}$ was attributed to the C–H stretching vibrations from both PVA and CMC. The existence of a significant peak of about 1650 $cm^{-1}$ in all spectra validated the amide-I (C=O) stretching vibration, indicative of the amide groups in the CMC polymer chains. A progressive reduction in the intensity of the amide-I band was observed with increasing concentrations of SrO–HA (2%, 4% and 10% w/v). This detection indicates possible interactions between the SrO–HA nanoparticles and the amide groups of the CMC polymer. These interactions may include modest intermolecular forces, including hydrogen bonding between the hydroxyl groups on the surface of SrO–HA nanoparticles and the amide groups

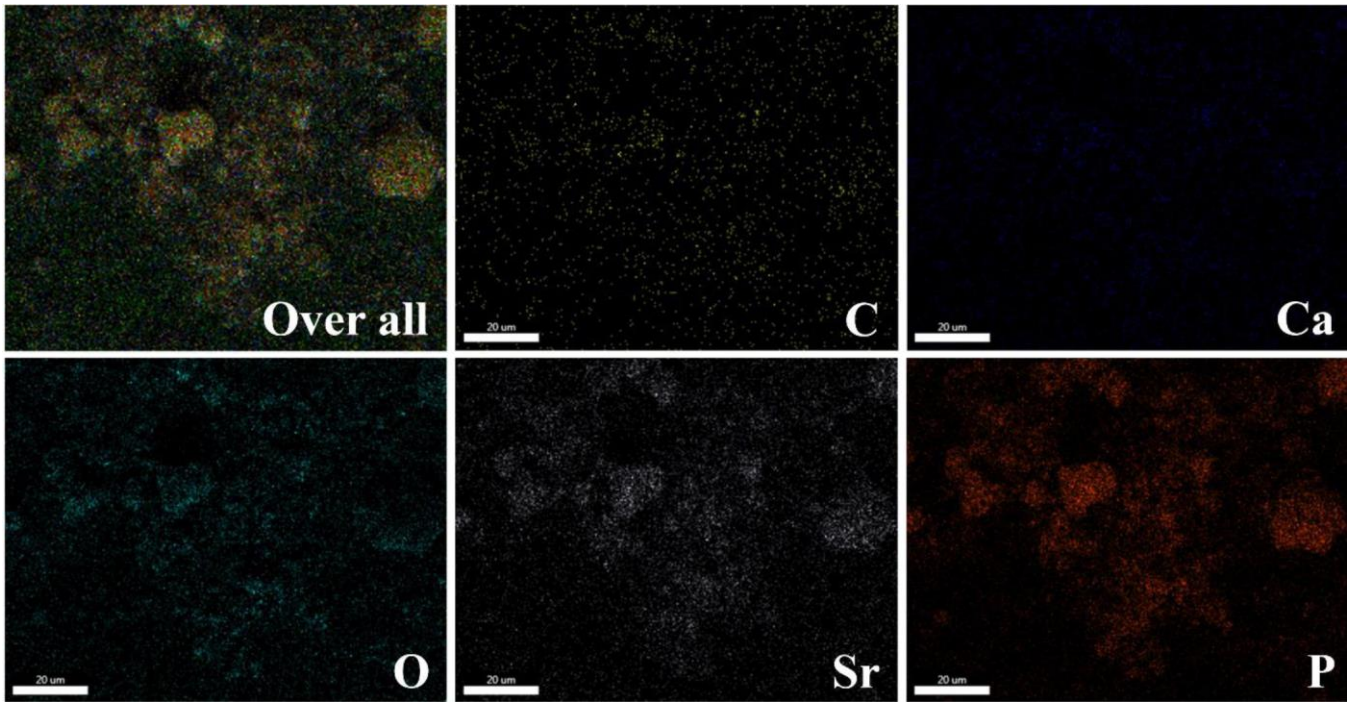


Fig. 3. Energy dispersive spectroscopy (EDS) analysis showing the distribution and concentration of surface elements in the hydrogels

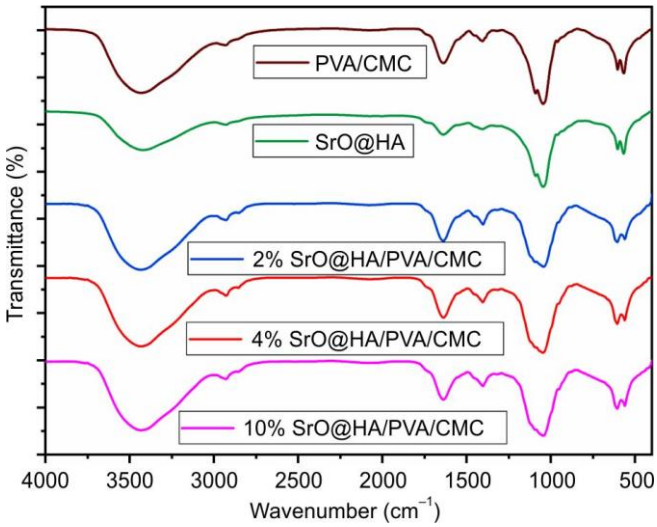


Fig. 4. Fourier transform infrared (FTIR) spectra of composite hydrogels with varying concentrations of PVA/CMC, SrO–HA, 2% SrO@HA/PVA/CMC, 4% SrO@HA/PVA/CMC and 10% SrO@HA/PVA/CMC

of CMC. Although, there was a significant reduction in the amide-I band intensity, FTIR analysis indicated that the addition of SrO–HA nanoparticles did not substantially modify the fundamental chemical structures of PVA and CMC in the hydrogel matrix. The distinctive peaks of both polymers were seen in all composite hydrogels, indicating the retention of their respective functional groups. These findings indicate that the inclusion of SrO–HA mostly affected the intermolecular interactions within the hydrogel network, rather than inducing substantial chemical alterations to the polymer chains [6,25,29].

**XRD studies:** The XRD pattern of pure HA exhibited characteristic peaks corresponding to the hexagonal hydroxyapatite phase, confirming its crystalline nature. The PVA/CMC hydrogel showed a broad, amorphous halo, indicating its non-crystalline structure. The composite hydrogels (2%, 4% and 10% SrO@HA/PVA/CMC) displayed a combination of peaks from both HA and PVA/CMC (Fig. 5). As the concentration of SrO@HA increased, the intensity of the HA peaks became more pronounced, suggesting a higher degree of crystallinity within the composite. Notably, the broad amorphous halo from PVA/CMC remained, indicating that the polymer matrix retained its amorphous nature. The SrO peaks were observed at higher concentrations, confirming the incorporation of Strontium Oxide. The increased intensity of HA peaks with higher SrO@HA concentrations suggests that the addition of SrO@HA enhances the overall crystallinity of

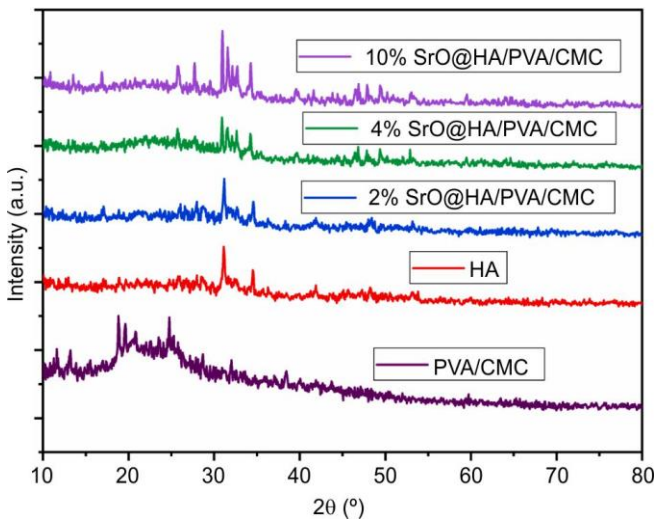


Fig. 5. X-ray diffraction (XRD) patterns of HA, PVA/CMC, 2% SrO@HA/PVA/CMC, 4% SrO@HA/PVA/CMC and 10% SrO@HA/PVA/CMC

the composite. This increased crystallinity may contribute to improved mechanical properties and bioactivity of the hydrogels. The presence of both crystalline HA and amorphous PVA/CMC provides a composite structure with a balance of strength and flexibility, potentially beneficial for tissue engineering applications.

**Porosity and density of SrO@HA/PVA/CMC:** A porosity study, performed using solvent displacement, indicated a progressive increase in porosity across the hydrogel samples: PVA/CMC (80.71%), 2% SrO@HA/PVA/CMC (81.88%), 4% SrO@HA/PVA/CMC (84.02%) and 10% SrO @HA/PVA/CMC (88.3%) (Fig. 6a). A tendency of increased porosity with higher SrO@HA concentration was observed; however, no statistically significant differences were identified among the samples. Simultaneously, hydrogel density showed a positive association with SrO@HA content, rising from 0.89 g $cm^{-3}$ in the PVA/CMC sample to 1.04 g $cm^{-3}$ in the 10% SrO@HA/PVA/CMC sample (Fig. 6b). The results correspond with SEM observations indicating that the interactions among the functional groups of PVA, CMC and the integrated SrO@ HA nanoparticles affected the development of the porous hydrogel structure.

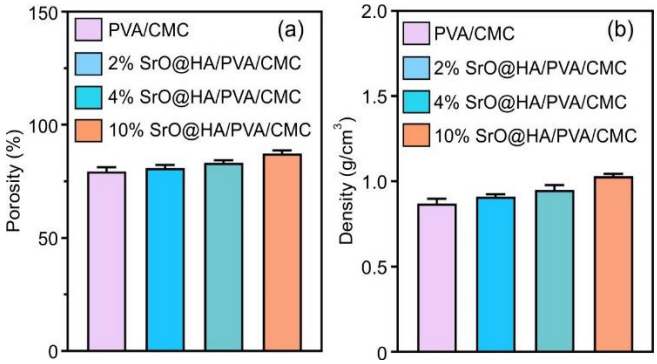


Fig. 6. (a) Porosity of SrO@HA/PVA/CMC composite hydrogels at different concentrations, (b) Density of SrO@HA/PVA/CMC composite hydrogels at different concentrations

The recorded porosity values (81.88-88.3%) for all hydrogel samples are within the physiological range of human cancellous bone (50-90%). This attribute is essential for bone tissue engineering applications since it emulates the natural porosity structure of bone and promotes cell infiltration, nutrition absorption and waste elimination [29]. The SEM results also disclosed a microporous architecture characterised by pore dimensions between 0.3 and 0.6 μm across all the prepared hydrogels. This microporous structure markedly lifts the specific surface area, improving protein adsorption and nutrient transport, which are critical for cell adhesion, proliferation and differentiation.

The incorporation of SrO@HA/PVA/CMC nanoparticles improves the bioactivity and mechanical characteristics of the hydrogels; nonetheless, it is crucial to recognize that augmenting the nanoparticle concentration which may affect cell-material interactions [32]. While the surface roughness might improve cell adhesion, excessive roughness or decreased pore size resulting from nanoparticle aggregation may impede cell migration and nutrient diffusion inside the 3D hydrogel matrix [33,34].

**Equilibrium swelling degree:** PVA/CMC and SrO@ HA/PVA/CMC hydrogels were immersed in ultrapure water to examine their equilibrium swelling behaviour. All hydrogels achieved equilibrium swelling within 24 h (Fig. 7). The PVA/CMC hydrogel demonstrated the highest equilibrium swelling degree, achieving approximately 1200% within 24 h. At 15 min, the PVA/CMC hydrogel exhibited a swelling ratio of approximately 800%, which increased to 950% at 20 min and further reached 1100% at 40 min. The addition of SrO@ HA nanoparticles markedly decreased the swelling capacity of the hydrogels. The SrO@HA/PVA/CMC samples at concentrations of 2%, 4% and 10% exhibited equilibrium swelling degrees of 950%, 875% and 750%, respectively, all attained within 24 h. The 2% SrO@HA/PVA/CMC hydrogel exhibited swelling rates of 600%, 700% and 850% at 15, 20 and 40 min, respectively. The 4% SrO@HA/PVA/CMC hydrogel demonstrated swelling rates of 500%, 600% and 750% at 15, 20 and 40 min, respectively. The 10% SrO@HA/ PVA/CMC hydrogel demonstrated swelling rates of 400%, 500% and 650% at 15, 20 and 40 min, respectively. The result demonstrates an inverse correlation between SrO@HA content and swelling capacity. The observed reduction in swelling behaviour with increasing SrO@HA content can be attributed to multiple factors. The incorporation of inorganic nanoparticles enhances the crosslinking density within the hydrogel network, thereby limiting the expansion of polymer chains during water uptake. Secondly, the inclusion of SrO@HA nanoparticles may decrease the hydrophilicity of the hydrogel matrix, thereby restricting the degree of water absorption. These findings align with prior research indicating a reduction in water absorption capacity as nanoparticle content in polymer-based hydrogels increases [35-38].

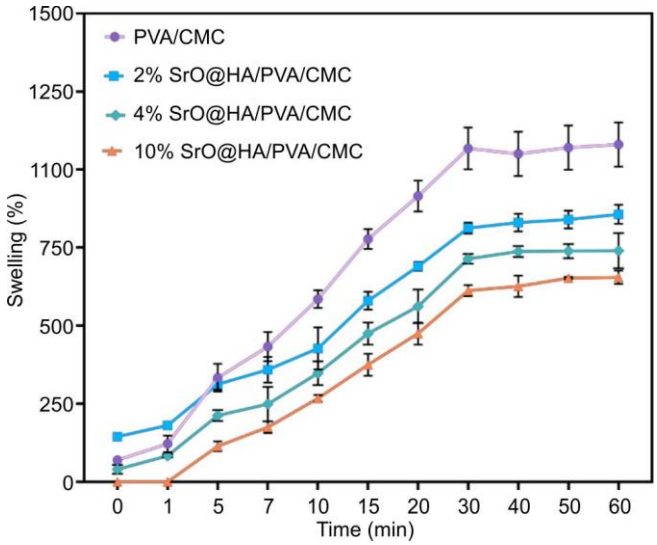


Fig. 7. Equilibrium swelling percentage of composite hydrogels with varying concentrations of SrO@HA/PVA/CMC

**pH detection:** The pH variation of the hydrogels in PBS solution was observed over 36 h. The PVA/CMC hydrogel demonstrated negligible pH fluctuations, consistently maintaining a pH 7.0 during the observation period. The SrO@HA/PVA/CMC hydrogels exhibited a gradual increase in pH. The final pH values for the 2%, 4% and 10% SrO@

HA/PVA/CMC samples were approximately 7.2, 7.5 and 8.0, respectively, after 24 h of immersion (Fig. 8). The observed gradual increase in pH for the SrO@HA/PVA/CMC hydrogels is attributable to the ion release from the SrO@HA nanoparticles. Strontium and hydroxyl ions released from SrO may elevate the local pH level. The dissolution of HA additionally releases hydroxyl ions, which contributes to the observed increase in pH. The observed pH changes have important implications for bone regeneration. A medium with a pH of 7.2-7.4 promotes osteogenic differentiation and mineralisation, whereas the mildly alkaline medium enhances the activity of alkaline phosphatase, an enzyme essential for bone formation. A slightly alkaline pH can improve the bioavailability of calcium and phosphate ions, which are essential for new bone matrix formation [39].

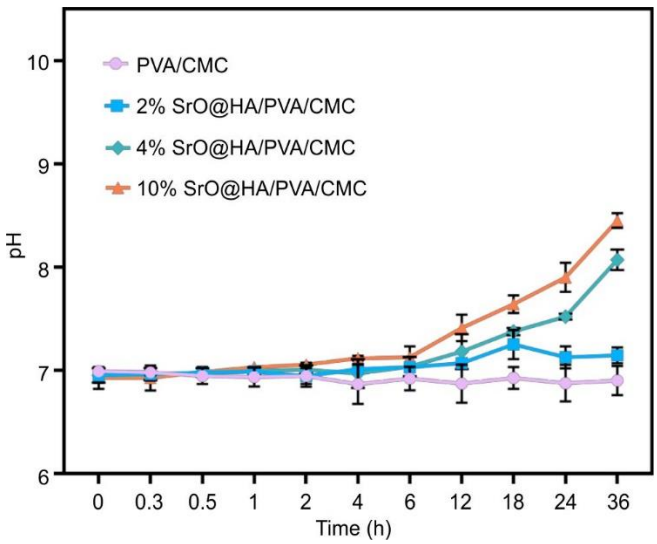


Fig. 8. pH changes of composite hydrogels with varying concentrations of SrO@HA/PVA/CMC

The observed gradual and moderate increase in pH in the SrO@HA/PVA/CMC hydrogels, especially in the 2% and 4% samples, indicates that these materials may develop an appropriate microenvironment for bone regeneration. Increased concentrations of SrO@HA (*e.g.* 10%) led to a significant rise in pH, which could adversely affect cell viability and tissue integration if the pH surpasses the physiological range.

**Ion release performance from SrO@HA/PVA/CMC hydrogel:** The *in vitro* release profiles of strontium ions from 2%, 4% and 10% SrO@HA/PVA/CMC hydrogels were assessed over 30 days. The 2% SrO@HA/PVA/CMC hydrogel demonstrated the fastest initial release, with around 20% of the total strontium content released in the first 24 h (Fig. 9). The 4% sample exhibited a marginally slower initial release, with around 15% of strontium released within the first 24 h. The 10% SrO@HA/PVA/CMC hydrogel exhibited the slowest initial release, with approximately 10% of strontium released during the first 24 h. The higher initial concentration of strontium ions available for release in the 2% sample accounts for this observation. The 10% SrO@HA/PVA/CMC hydrogel exhibited a more sustained release profile. The release was slow at the beginning; however, the 10% SAMPLE showed a steady release of strontium ions over 30 days, reaching about

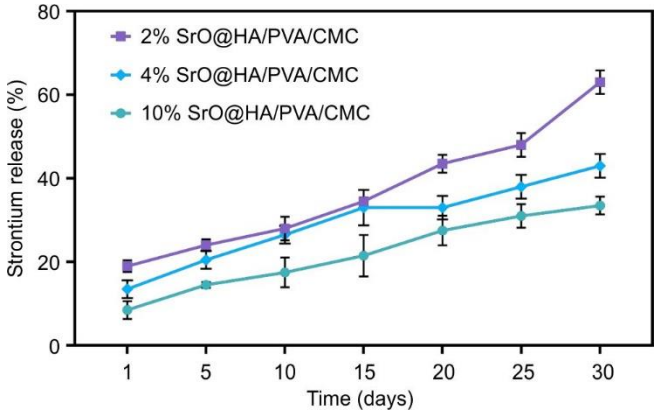


Fig. 9. Strontium ion release profile from composite hydrogels over 30 days

35% total release by the end of the study. The higher amount of nanoparticles in the 10% sample likely helped control and extend the release. The interaction between the nanoparticles and the hydrogel reduced the sudden initial release and allowed a more sustained and gradual release over time. All samples demonstrated a progressive decline in strontium ion release over time, achieving a plateau phase within 20 to 25 days. The sustained release profile is essential for the optimal bone regeneration outcomes.

The proliferation and differentiation of bone marrow mesenchymal stem cells (BMSCs) into mature bone-forming cells (osteoblasts) are stimulated through the activation of various signalling pathways such as MAPK and ERK pathways [40]. SrO promotes bone formation through the augmentation of bone mineral density and the stimulation of osteoblast activity. Moreover, it can regulate bone resorption by inhibiting osteoclast activity, which is responsible for bone degradation [29,41,42]. The continuous release of strontium ions from the SrO@HA/PVA/CMC hydrogels offers a regulated stimulus for bone regeneration.

**Moisture level:** The moisture content of hydrogels was assessed through vacuum drying at 70 ºC. The PVA/CMC hydrogel demonstrated the highest initial moisture content, approximately 92.25% at day zero. The addition of SrO@HA nanoparticles markedly decreased the initial moisture content. The initial moisture contents for the 2%, 4% and 10% SrO @HA/PVA/CMC samples were approximately 90%, 88% and 85%, respectively (Fig. 10). All samples demonstrated a progressive reduction in moisture content throughout the 60 min observation period, achieving equilibrium within 46 min of drying at each time interval. The reduction in moisture content can be ascribed to multiple factors, for example, (i) the inclusion of SrO@HA nanoparticles in the hydrogel matrix likely diminished the available pore space within the hydrogel network, thereby restricting the volume of water that can be absorbed and retained; (ii) competitive hydrogen bonding occurs as the hydroxyl groups on the surface of SrO@HA nanoparticles establish hydrogen bonds with the hydrophilic groups, such as hydroxyl groups, present in the PVA/CMC polymer matrix. The competitive hydrogen bonding diminishes the availability of water-binding sites in the hydrogel, resulting in reduced water uptake; and (iii) the interaction of SrO@HA nanoparticles with polymer chains can induce cross-linking in the hydrogel network. The cross-linking process

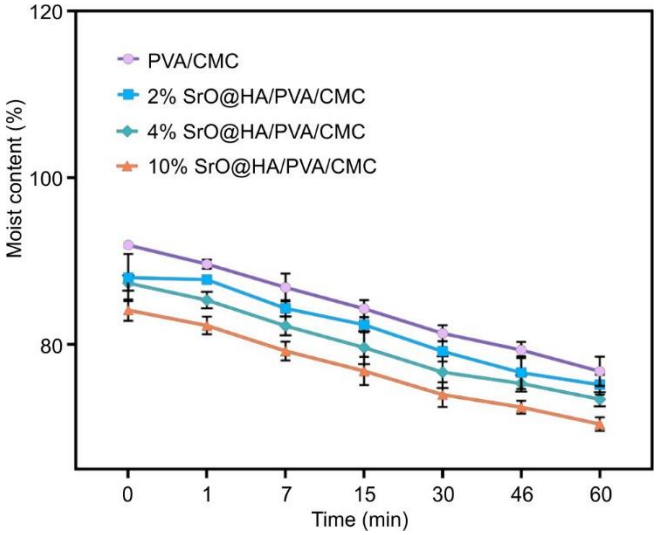


Fig. 10. Water content of composite hydrogels with varying concentrations of SrO@HA/PVA/CMC

restricts the swelling and expansion of polymer chains, thereby limiting the water absorption and retention capacity of the hydrogel.

The decrease in moisture content with increasing SrO@HA concentration indicates that these effects are contingent upon the nanoparticle loading in the hydrogel. This finding is consistent with prior research indicating a reduction in water absorption capacity as nanoparticle content in polymer-based hydrogels increases. The decreased moisture content may affect the mechanical properties of hydrogels, including compressive strength and stiffness, which are essential for load-bearing applications in bone tissue engineering [37,43,44]. Furthermore, the reduced moisture content may impact the degradation rate of hydrogels, which could subsequently influence the release kinetics of bioactive ions, including strontium and calcium, as well as the overall biodegradation profile within the physiological environment.

***In vitro* mineralisation analysis:** The hydrogel's biomineralisation characteristics were assessed by submerging them in SBF for 14 days at 37 ºC. After incubation and extensive washing, the hydrogels underwent SEM analysis combined with EDX to evaluate the development of apatite-like mineral deposits on their surfaces and ascertain their elemental composition.

The PVA/CMC hydrogel demonstrated low apatite production after 14 days of immersion in SBF, with insignificant calcium content identified using EDX analysis (Fig. 11). Conversely, the SrO@HA/PVA/CMC hydrogels exhibited differing levels of apatite deposition and calcium concentration. The 2% SrO@HA/PVA/CMC sample demonstrated considerable apatite production, shown by tiny, distinct apatite crystals on the hydrogel surface, with an estimated calcium concentration of around 5-8% (atomic %). The 4% SrO@HA /PVA/CMC sample exhibited a notable enhancement in apatite deposition, characterised by bigger and more numerous apatite crystals on the hydrogel surface, with an estimated calcium concentration of 10-15% (atomic %). The 10% SrO @HA/ PVA/CMC sample had the greatest degree of apatite production, characterised by a thick layer of apatite crystals enveloping the majority of the hydrogel surface, with an estimated calcium content of 15-20% (atomic %).

The results indicate that the integration of SrO@HA nanoparticles markedly improves the biomineralisation characteristics of the hydrogels. The incorporation of SrO and HA in the composite likely serves as nucleation sites for apatite crystal formation, facilitating the deposition of calcium and phosphate ions from the SBF onto the hydrogel surface [45]. Moreover, the liberation of strontium ions from the SrO@HA nanoparticles may enhance the biomineralisation by affecting the local ionic milieu and facilitating the development of a more stable apatite layer [46].

By varying the loading of nanoparticles in the matrix of the hydrogel, the biomineralisation ability of the hydrogels may be regulated, as shown by the observed increase in calcium content and apatite production with increasing SrO @HA concentration. Excessive nanoparticle loading may result in adverse consequences, including diminished cell viability or impaired nutrient transport. Thus, adjusting the SrO@HA concentration is essential for attaining a balance between improved biomineralisation and advantageous biological performance.

***In vitro* biocompatibility assay:** Cell viability was evaluated through the CCK-8 assay following the co-culture of rBMSCs with extracts from PVA/CMC, 2% SrO@HA/PVA/CMC, 4% SrO@HA/PVA/CMC and 10% SrO@HA/PVA/CMC hydrogels over periods of 1, 4 and 7 days (Fig. 12). Slight increases in cell viability were observed in the PVA/CMC and 2% SrO@HA/PVA/CMC samples on day 1 relative to the control; however, these differences lacked statistical significance. The 4% and 10% SrO@HA/PVA/CMC samples demonstrated significantly greater cell viability compared to the control sample. The pattern persisted, with all SrO@HA-doped samples exhibiting significantly higher cell viability compared to the control on days 4 and 7. The enhancement in cell viability observed in the SrO@HA/PVA/CMC samples indicates that the incorporation of SrO@HA nanoparticles significantly enhances the biocompatibility of the hydrogel. The improved cell viability results from multiple factors, notably the gradual release of strontium ions, which promote cell proliferation and differentiation through the stimulation of various cellular signaling path-ways [47,18]. The inclusion of SrO@HA nanoparticles can enhance the biomimetic characteristics of the hydrogel, replicating the mineral composition of natural bone and fostering a more conducive microenvironment for cell adhesion, growth and differentiation. The hydrogel matrix serves as a reservoir for the sustained release of strontium ions and other bioactive factors from the nanoparticles, facilitating continuous stimulation of cellular activity [49,50]. The observed dose-dependent effect indicates that higher concentrations of SrO@HA (4% and 10%) result in more significant increases in cell viability on day 1. It suggests that the initial burst release of ions and particles from these concentrations is critical for early cell proliferation. The continuous release of bioactive factors from all SrO@HA-doped samples throughout the 7-day culture period demonstrates that the biocompatibility and cell-supporting properties of these hydrogels are preserved. The PVA/CMC sample exhibited a marginal increase in cell

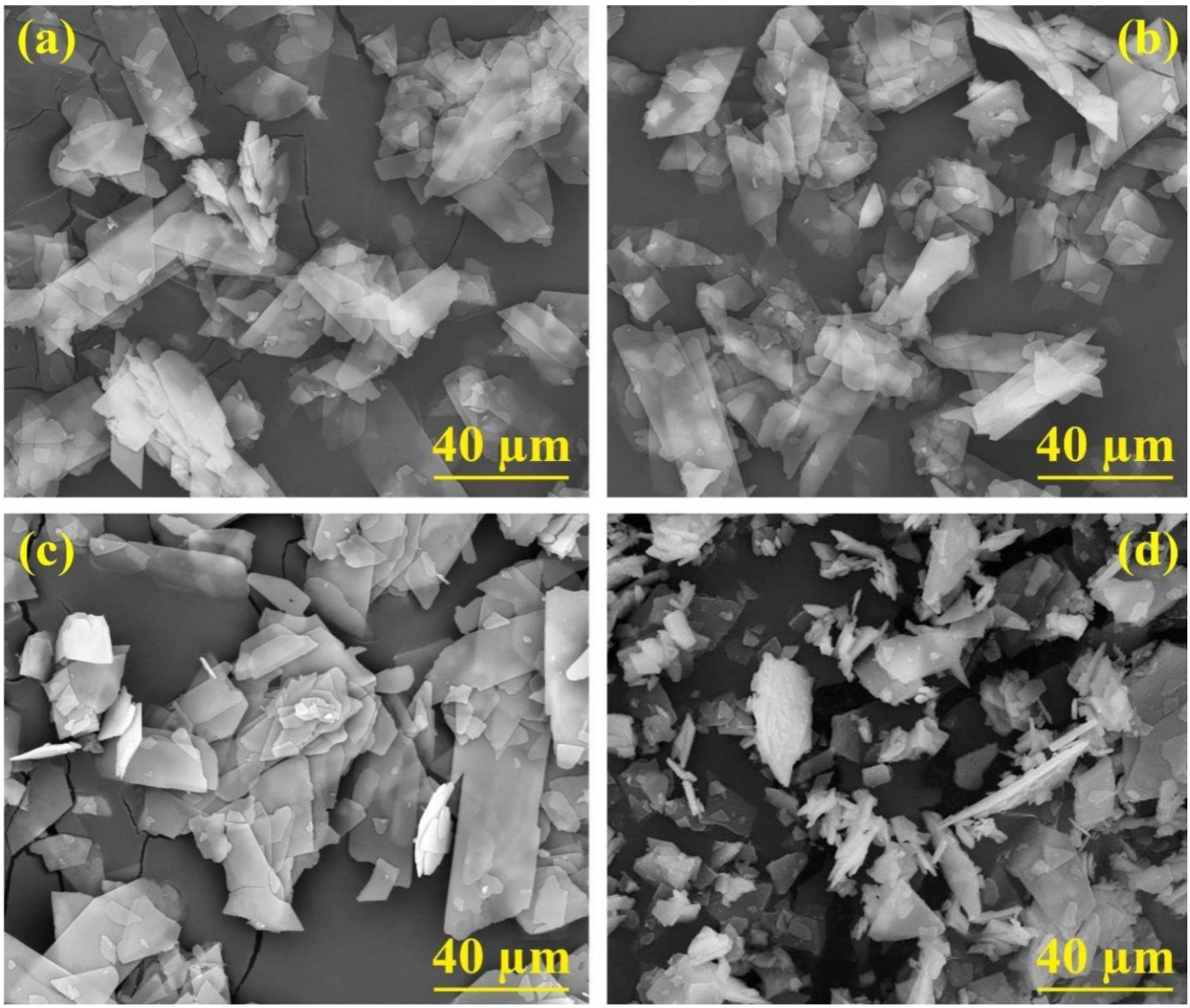


Fig. 11. *In vitro* mineralisation analysis of SrO@HA/PVA/CMC composite hydrogels at different concentrations

viability relative to the control; however, this difference did not achieve statistical significance, indicating a restricted influence of the base hydrogel on cell proliferation. According to the results, SrO@HA nanoparticles greatly increase cell survival when added to PVA/CMC hydrogels, suggesting high biocompatibility and the possibility of better tissue integration in bone regeneration applications.

**AO/EtBr staining:** To assess rBMSC viability during osteogenic differentiation in different hydrogels (PVA/CMC, 2% SrO@HA/PVA/CMC, 4% SrO@HA/PVA/CMC and 10% SrO@HA/PVA/CMC), an AO/EtBr staining test was performed (Fig. 13). In comparison to the PVA/CMC control, the 2% SrO@HA/PVA/CMC sample had much superior cell vitality across the 7-day differentiation period, indicating that the addition of 2% SrO@HA improves cell survival while preserving biocompatibility. The 4% and 10% SrO@HA/PVA/CMC samples exhibited cell viability similar to the control sample, suggesting that the 10% SrO@HA concentration did not display substantial cytotoxicity under these experimental circumstances.

**ALP staining:** The activity of ALP, an early indicator of osteogenic differentiation, was evaluated in rBMSCs cultured in conditioned media over periods of 1 and 2 weeks (Fig. 14). During week 1, all samples displayed low cell density; however, the SrO@HA/PVA/CMC samples demonstrated significantly deeper purple staining relative to the PVA/CMC samples, indicating increased ALP activity. By week 2, there was a significant increase in cell density across all samples. The SrO@HA/PVA/CMC samples, especially those with 4% and 10% SrO@HA/PVA/CMC, exhibited darker purple staining in comparison to the PVA/CMC sample, suggesting an enhancement in ALP activity. The increased ALP activity in the SrO@HA/PVA/CMC samples likely results from the synergistic interactions between SrO@HA nanoparticles and the hydrogel matrix. SrO@HA nanoparticles can release strontium ions, which are recognised for their role in promoting osteoblast proliferation and differentiation. Moreover, the 3D hydrogel structure facilitates an environment suitable for cell attachment, growth and matrix deposition. The observed dose-dependent increase in ALP activity with escalating SrO@HA

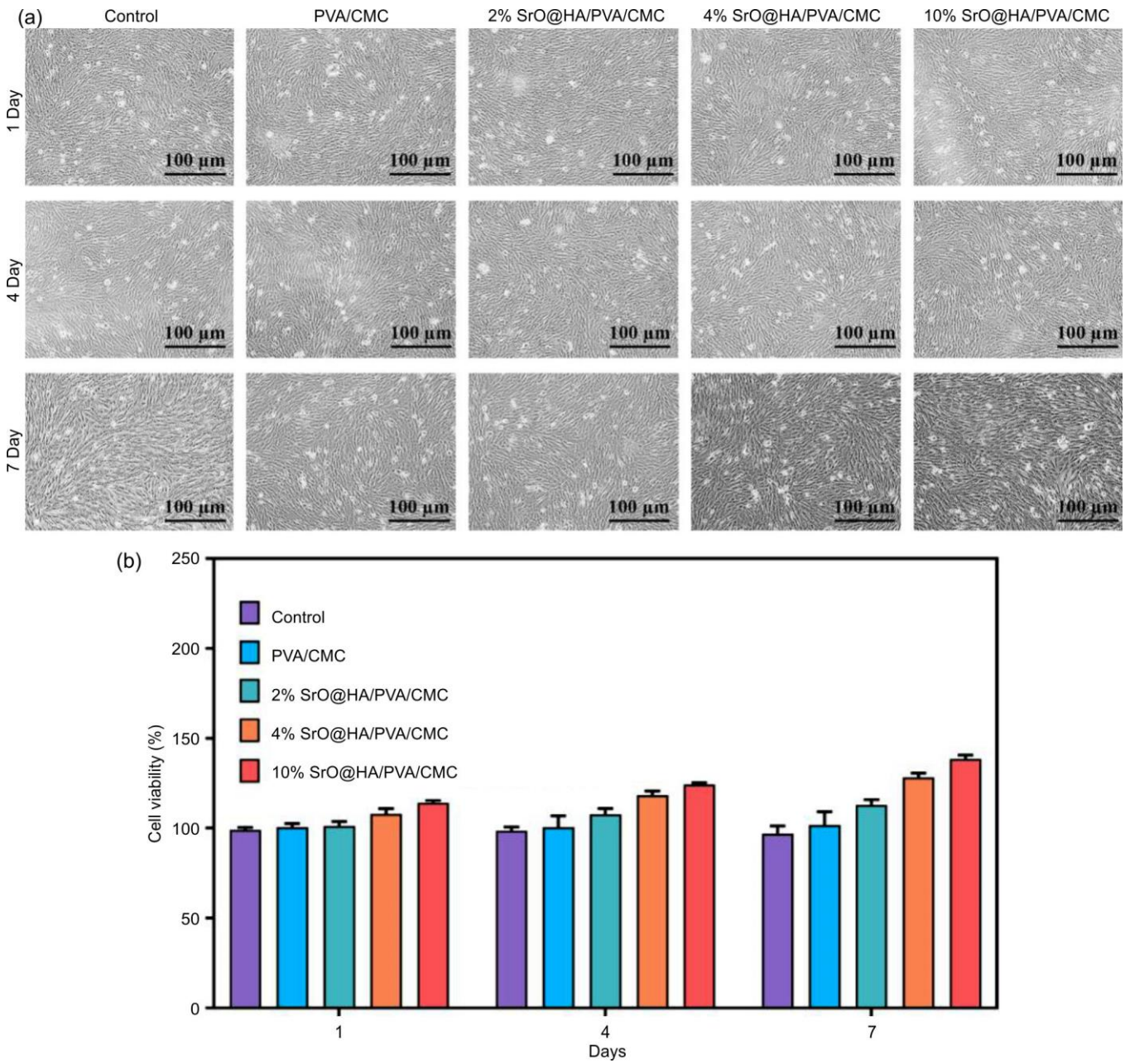


Fig. 12. *In vitro* biocompatibility assays of composite hydrogels with varying concentrations of SrO@HA/PVA/CMC at 1, 4 and 7 days

concentration (up to 4%) suggests an optimal range for the incorporation of nanoparticles. The observed increase in ALP activity indicates that SrO@HA/PVA/CMC hydrogels may effectively facilitate bone regeneration through the stimulation of osteogenic differentiation in rBMSCs.

**Alizarin red staining:** Following a two-week culture period, a significat enhancement in Alizarin red S staining was detected in the SrO@HA/PVA/CMC groups relative to the PVA/CMC control group (Fig. 15). The staining intensity increased progressively with higher concentrations of SrO@HA, with the 4% and 10% SrO@HA/PVA/CMC samples demonstrating the most significant mineralisation. This observation indicates that the inclusion of SrO@HA nanoparticles markedly improves the mineralisation capacity of rBMSCs in the hydrogel environment. The increased mineralisation observed in SrO@HA/PVA/CMC samples results from the multiple factors, especially the sustained release of strontium ions that promote osteoblast differentiation and matrix mineralisation. The 3D structure of the hydrogel develops an matrix setting that promotes cell-cell and cell-matrix interactions, thereby facilitating the deposition of a calcium-rich extracellular matrix. The observed enhancement in alizarin red S staining indicates that SrO@HA/PVA/CMC hydrogels effectively promote bone regeneration by stimulating significant mineralisation of the extracellular matrix, which is essential for bone tissue formation.

## Conclusion

This study examined the efficacy of SrO@HA/PVA/CMC composite hydrogels in bone tissue engineering applications.

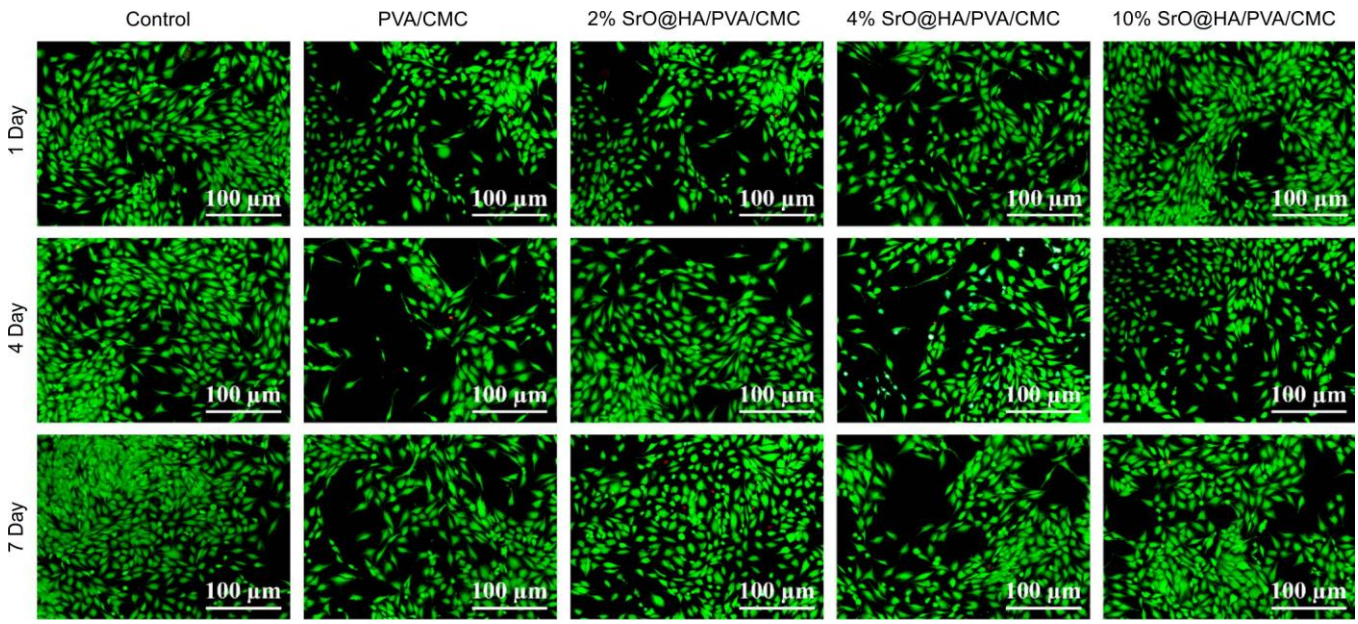


Fig. 13. Acridine orange/ethidium bromide (AO/EtBr) staining of composite hydrogels with varying concentrations of SrO@HA/PVA/CMC at 1, 4 and 7 days

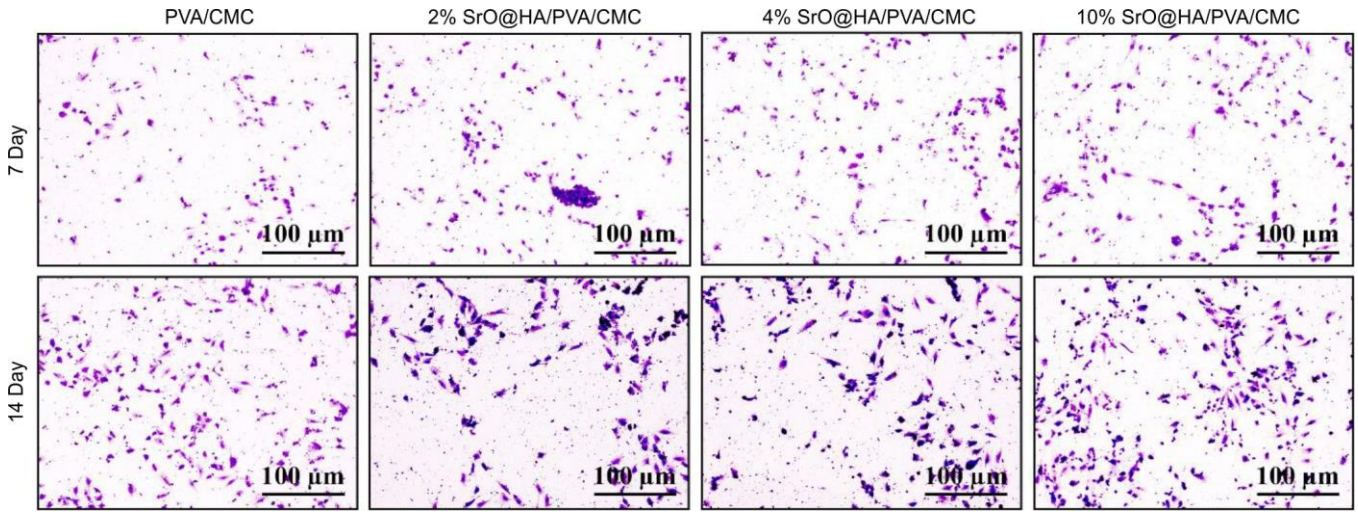


Fig. 14. Alkaline phosphatase (ALP) staining of composite hydrogels with varying concentrations of SrO@HA/PVA/CMC at 7 and 14 days

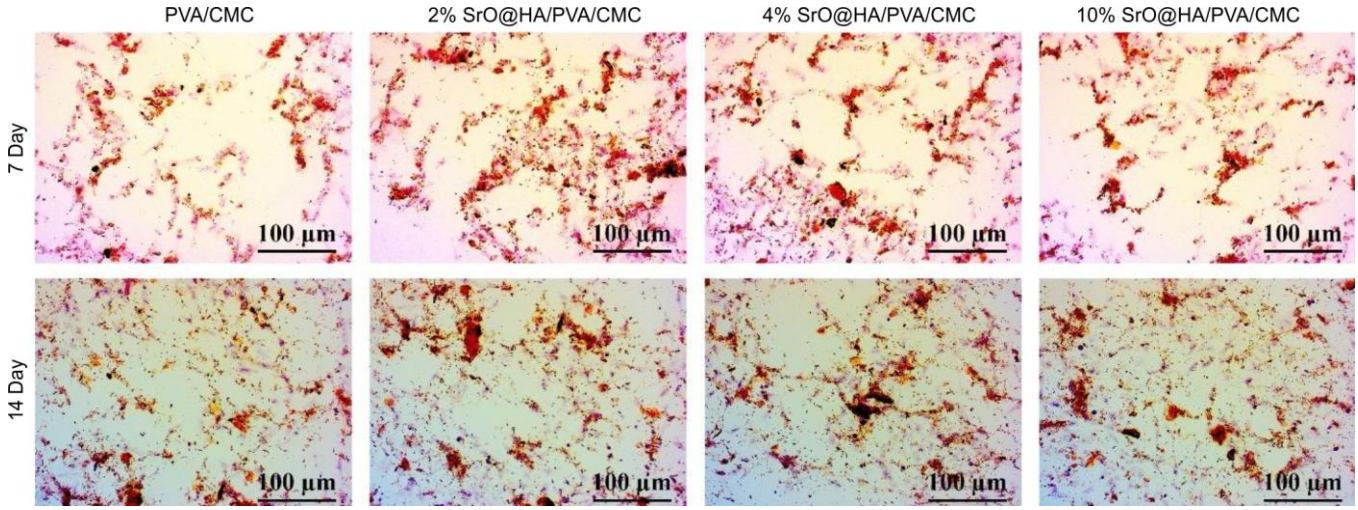


Fig. 15. Alizarin red S (ARS) staining of composite hydrogels with varying concentrations of SrO@HA/PVA/CMC at 7 and 14 days

The hydrogels were fabricated using a combination of magnetic stirring-ion exchange and freeze-thaw physical cross-linking techniques. The integration of SrO@HA nanoparticles into the PVA/CMC matrix led to the development of interconnected porous structures exhibiting regulated swelling properties and prolonged release of strontium ions. *In vitro* studies indicated high biocompatibility, with the hydrogels facilitating rBMSC proliferation and enhancing osteogenic differentiation, as shown by elevated ALP activity and significant mineralisation. The improved osteogenic differentiation and mineralisation result from the combined effects of strontium ion release, the biomimetic characteristics of SrO @HA nanoparticles and the 3D porous structure of the hydrogel. The findings indicate that SrO@HA/PVA/CMC hydrogels have considerable potential for applications in bone tissue regeneration.

## CONFLICT OF INTEREST

The authors declare that there is no conflict of interests regarding the publication of this article.

## DECLARATION OF AI-ASSISTED TECHNOLOGIES

During the preparation of this manuscript, the authors used an AI-assisted tool(s) to improve the language. The authors reviewed and edited the content and take full responsibility for the published work.

## REFERENCES


1. A.S. Priya, R. Premanand, I. Ragupathi, V.R. Bhaviripudi, R. Aepuru, K. Kannan and K. Shanmugaraj, *J. Compos. Sci.*, **8**, 457 (2024); https://doi.org/10.3390/jcs8110457
2. U.T. Sampath, Y.C. Ching, C.H. Chuah, R. Singh and P.C. Lin, *Cellulose*, **24**, 2215 (2017); https://doi.org/10.1007/s10570-017-1251-8
3. S.C. Sutradhar, H. Shin, W. Kim and H. Jang, *Gels*, **11**, 918 (2025); https://doi.org/10.3390/gels11110918
4. H. Kaur, B. Gogoi, I. Sharma, D.K. Das, M.A. Azad, D.D. Pramanik and A. Pramanik, *Mol. Pharmaceutics*, **21**, 4827 (2024); https://doi.org/10.1021/acs.molpharmaceut.4c00595
5. W. Kruczkowska, K.K. Kłosiński, K.H. Grabowska, J. Gałęziewska, P. Gromek, M. Kciuk, Ż. Kałuzińska-Kołat, D. Kołat and R.A. Wach, *Molecules*, **29**, 4360 (2024); https://doi.org/10.3390/molecules29184360
6. D. Tzaneva, A. Simitchiev, N. Petkova, V. Nenov, A. Stoyanova and P. Denev, *J. Appl. Pharm. Sci.*, **7**, 070 (2017); https://doi.org/10.7324/JAPS.2017.71010
7. Y. Liu, J. Zhang and D. Wang, *Chem. Eng. J.*, **508**, 160946 (2025); https://doi.org/10.1016/j.cej.2025.160946
8. M.F.A. Cutiongco, R.K.T. Choo, N.J.X. Shen, B.M.X. Chua, E. Sju, A.W.L. Choo, C. Le Visage and E.K.F. Yim, *Front. Bioeng. Biotechnol.*, **3**, 3 (2015); https://doi.org/10.3389/fbioe.2015.00003
9. P. Ma, W. Wu, Y. Wei, L. Ren, S. Lin and J. Wu, *Mater. Des.*, **207**, 109865 (2021); https://doi.org/10.1016/j.matdes.2021.109865
10. N.H. Ngadiman, N.M. Yusof, A. Idris, E. Fallahiarezoudar and D. Kurniawan, *Polymers*, **10**, 353 (2018); https://doi.org/10.3390/polym10040353
11. S.P. Gherman, G. Biliuță, A. Bele, A.M. Ipate, R.I. Baron, L. Ochiuz, A.F. Șpac and D.E. Zavastin, *Gels*, **9**, 122 (2023); https://doi.org/10.3390/gels9020122
12. L. Gao, Y. Hou, H. Wang, M. Li, L. Ma, Z. Chu, I.S. Donskyi and R. Haag, *Angew. Chem.*, **134**, 202201563 (2022); https://doi.org/10.1002/ange.202201563
13. Z. Chen, Y. Liu, J. Huang, M. Hao, X. Hu, X. Qian, J. Fan, H. Yang and B. Yang, *Polymers*, **14**, 3404 (2022); https://doi.org/10.3390/polym14163404
14. K. Zhang, Y. Zhu and W. Wang, *BMC Musculoskelet. Disord.*, **24**, 427 (2023); https://doi.org/10.1186/s12891-023-06405-x
15. L. Vaiani, A. Boccaccio, A.E. Uva, G. Palumbo, A. Piccininni, P. Guglielmi, S. Cantore, L. Santacroce, I.A. Charitos and A. Ballini, *J. Funct. Biomater.*, **14**, 146 (2023); https://doi.org/10.3390/jfb14030146
16. M. Grau, C. Seiler, L. Roland, J. Matena, C. Windhövel, M. Teske, H. Murua Escobar, M. Lüpke, H. Seifert, N.C. Gellrich, H. Haferkamp and I. Nolte, *Materials*, **11**, 6 (2017); https://doi.org/10.3390/ma11010006
17. A.H. Yusop, A.A. Bakir, N.A. Shaharom, M.R. Abdul Kadir and H. Hermawan, *Int. J. Biomater.*, **2012**, 641430 (2012); https://doi.org/10.1155/2012/641430
18. G.K. Manne, K. Srinivasan, G.N. Obularajugari, R. Kumar, P. Pathi, N. Hanumanthappa, G.K. Pitchika, S. Battana and R. Mandala, *J. Appl. Polym. Sci.*, **142**, 160946 (2025); https://doi.org/10.1002/app.56811
19. F. Fendi, B. Abdullah, S. Suryani, I. Raya, D. Tahir and I. Iswahyudi, *Polym. Bull.*, **81**, 1097 (2024); https://doi.org/10.1007/s00289-023-04794-6
20. F. Fendi, B. Abdullah, S. Suryani, A.N. Usman and D. Tahir, *Bone*, **183**, 117075 (2024); https://doi.org/10.1016/j.bone.2024.117075
21. M. Gong, Q. Zhao, L. Dai, Y. Li and T.J. Jiang, *Asian Ceram. Soc.*, **5**, 160 (2017); https://doi.org/10.1016/j.jascer.2017.04.001
22. C. Vibha and P.P. Lizymol, *Mater. Lett.*, **197**, 63 (2017); https://doi.org/10.1016/j.matlet.2017.03.098
23. J. You, Y. Zhang and Y. Zhou, *Front. Bioeng. Biotechnol.*, **10**, 928799 (2022); https://doi.org/10.3389/fbioe.2022.928799
24. M.Y. Almashnowi, M.S. Rashid, S.K. Ali, W.M. Alamier and A.M. Bakry, *J. Mater. Sci. Mater. Electron.*, **35**, 2199 (2024); https://doi.org/10.1007/s10854-024-13961-y
25. J. Wang, J. Guan, F. Jia, Z. Tian, L. Song, L. Xie, P. Han, H. Lin, H. Qiao, X. Zhang and Y. Huang, *Int. J. Biol. Macromol.*, **287**, 138608 (2025); https://doi.org/10.1016/j.ijbiomac.2024.138608
26. X. Cheng, L. Shao, H. Shen and H. Liu, *Chin. J. Tissue Eng. Res.*, **29**, 4639 (2025); https://doi.org/10.12307/2025.464
27. J. Liuyun, L. Yubao and X. Chengdong, *J. Biomed. Sci.*, **16**, 65 (2009); https://doi.org/10.1186/1423-0127-16-65
28. Z. Ma, D.M. Nelson, Y. Hong and W.R. Wagner, *Biomacromolecules*, **11**, 1873 (2010); https://doi.org/10.1021/bm1004299
29. C.I. Codrea, D. Baykara, R.A. Mitran, A.C. Koyuncu, O. Gunduz and A. Ficai, *Polymers*, **16**, 1932 (2024); https://doi.org/10.3390/polym16131932
30. G.D. Cha, W.H. Lee, C. Lim, M.K. Choi and D.H. Kim, *Nanoscale*, **12**, 10456 (2020); https://doi.org/10.1039/D0NR01456G
31. S. Wu, Y. Lai, X. Zheng and Y. Yang, *Heliyon*, **10**, e31638 (2024); https://doi.org/10.1016/j.heliyon.2024.e31638
32. A. Kakuta, T. Tanaka, M. Chazono, H. Komaki, S. Kitasato, N. Inagaki, S. Akiyama and K. Marumo, *Biomater. Res.*, **23**, 12 (2019); https://doi.org/10.1186/s40824-019-0161-2
33. I. Chiulan, A.N. Frone, C. Brandabur and D.M. Panaitescu, *Bioengineering*, **5**, 2 (2017); https://doi.org/10.3390/bioengineering5010002
34. J.M. Singelyn and K.L. Christman, *Macromol. Biosci.*, **11**, 731 (2011); https://doi.org/10.1002/mabi.201000423
35. C. Amante, V. Andretto, A. Rosso, G. Augusti, S. Marzocco, G. Lollo and P. Del Gaudio, *Drug Deliv. Transl. Res.*, **13**, 1343 (2023); https://doi.org/10.1007/s13346-022-01257-9
36. A. Bhowmick, N. Pramanik, T. Mitra, A. Gnanamani, M. Das and P.P. Kundu, *New J. Chem.*, **41**, 7524 (2017); https://doi.org/10.1039/C7NJ01246B
37. K. Zhang, Y. Liu, Z. Zhao, X. Shi, R. Zhang, Y. He, H. Zhang and W. Wang, *Int. J. Nanomed.*, **2024**, 651 (2024); https://doi.org/10.2147/IJN.S434060

38. J.W. Guo, C.F. Wang, J.Y. Lai, C.H. Lu and J.K. Chen, *J. Membr. Sci.*, **618**, 118732 (2021); https://doi.org/10.1016/j.memsci.2020.118732
39. M. Song, B. Yu, S. Kim, M. Hayashi, C. Smith, S. Sohn, E. Kim, J. Lim, R.G. Stevenson and R.H. Kim, *Dent. Clin. North Am.*, **61**, 93 (2017); https://doi.org/10.1016/j.cden.2016.08.008
40. L.-F. Zhuang, H.-H. Jiang, S.-C. Qiao, C. Appert, M.-S. Si, Y.-X. Gu, and H.-C. Lai, *J. Biomed. Mater. Res. A*, **100**, 125 (2012); https://doi.org/10.1002/jbm.a.33247
41. Q. Wu, L. Hu, R. Yan, J. Shi, H. Gu, Y. Deng, R. Jiang, J. Wen and X. Jiang, *Bone Res.*, **10**, 55 (2022); https://doi.org/10.1038/s41413-022-00224-x
42. Y. Luo, H. Liu, Y. Zhang, Y. Liu, S. Liu, X. Liu and E. Luo, *Biomater. Sci.*, **11**, 7268 (2023); https://doi.org/10.1039/D3BM01146A
43. A. Chhatri, J. Bajpai and A.K. Bajpai, *Biomatter*, **1**, 189 (2011); https://doi.org/10.4161/biom.19005
44. N. Bahadoran Baghbadorani, T. Behzad, M.H. Karimi Darvanjooghi and N. Etesami, *Cellulose*, **27**, 9927 (2020); https://doi.org/10.1007/s10570-020-03511-0
45. P. Habibovic, F. Barrère, C.A. Van Blitterswijk, K. de Groot and P. Layrolle, *J. Am. Ceram. Soc.*, **85**, 517 (2002); https://doi.org/10.1111/j.1151-2916.2002.tb00126.x
46. D. Cheng, R. Ding, X. Jin, Y. Lu, W. Bao, Y. Zhao, S. Chen, C. Shen, Q. Yang and Y. Wang, *ACS Appl. Mater. Interfaces*, **15**, 19951 (2023); https://doi.org/10.1021/acsami.3c00655
47. Z. Zhang, N. Gong, Y. Wang, L. Xu, S. Zhao, Y. Liu and F. Tan, *Biol. Trace Elem. Res.*, **203**, 1922 (2025); https://doi.org/10.1007/s12011-024-04303-4
48. J. Alves Côrtes, J. Dornelas, F. Duarte, M.R. Messora, C.F. Mourão and G. Alves, *Appl. Sci.*, **14**, 7566 (2024); https://doi.org/10.3390/app14177566
49. Y. Zhang, T. Yu, L. Peng, Q. Sun, Y. Wei and B. Han, *Front. Pharmacol.*, **11**, 622 (2020); https://doi.org/10.3389/fphar.2020.00622
50. C. Duan, H. Jiang, S. Zhang, Y. Wang, P. Liu, B. Xu, W. Tian and B. Han, *Biomater. Sci.*, **13**, 1449 (2025); https://doi.org/10.1039/D4BM01260G